The Astrophysical Journal Letters, 943:L25 (7pp), 2023 February 1 https://doi.org/10.3847/2041-8213/acb546

Discovery of a Spatially and Kinematically Resolved 55 kpc Scale Superbubble Inflated by an Intermediate-redshift Non-BAL Quasar

Qinyuan Zhao[1] and Junfeng Wang[1]
Department of Astronomy, Xiamen University, Xiamen, Fujian 361005, People's Republic of China; zqy94070@xmu.edu.cn, jfwang@xmu.edu.cn
Received 2022 November 28; revised 2023 January 20; accepted 2023 January 22; published 2023 February 1

Abstract

We report on the discovery of a rare case of spatially and kinematically resolved galactic-scale outflow at intermediate redshift based on VLT/MUSE optical integral field spectroscopic observation of the quasar HE 0238–1904. This classical non–broad absorption line quasar at $z = 0.631$ remains underexplored in its optical emission lines, though its UV absorption lines are well studied. We identify a superbubble driven by HE 0238−1904 from the emission line morphology, line ratio diagnostics, and kinematics showing a one-sided outflow reaching a projected distance of $R \sim 55$ kpc from the nucleus. The bulk of the ionized gas, with a characteristic mass $M \sim 10^8\,M_\odot$, is blueshifted by $v \approx 700$ km s^{-1} with respect to the quasar systemic velocity. The outflows detected using the absorption and emission lines are likely stratified components of different spatial scale and velocity in the ionized phase outflow. Although feedback in HE 0238–1904 is taking place on kiloparsec scales, the kinetic power of the outflow at 55 kpc ($\ll 0.1\%\ L_{\rm bol}$) implies that it is inadequate to effectively regulate the evolution of the host galaxy at this large scale.

Unified Astronomy Thesaurus concepts: Active galactic nuclei (16); Superbubbles (1656); Galaxy winds (626)

1. Introduction

Modern galaxy formation theory strongly suggests that there is a fundamental connection between the supermassive black holes (SMBHs) residing in galaxy centers and the formation and evolution of their host galaxies (Kormendy & Ho 2013). Theoretical studies and simulations show that active galactic nucleus (AGN) feedback can provide an explanation for a variety of observations, from the chemical enrichment of the intergalactic medium to the self-regulation of the growth of the SMBHs and the galactic bulge (e.g., Ferrarese & Merritt 2000; Gebhardt et al. 2000; Tremaine et al. 2002; Di Matteo et al. 2005; Hopkins & Elvis 2010). Powerful outflows driven by AGN have been invoked as one of the main conveyors, so that SMBH activity has a controlling effect on shaping the global properties of the host galaxies (Tabor & Binney 1993; Silk & Rees 1998; Springel et al. 2005; Veilleux et al. 2005; Croton et al. 2006; Hopkins et al. 2006; Choi et al. 2012; Veilleux et al. 2020).

In the past several years, AGN-driven outflows extending to kiloparsec scales have been resolved in ionized, atomic, and molecular gas around both radio-loud (e.g., Nesvadba et al. 2006, 2008; Vayner et al. 2021a) and radio-quiet (e.g., Nesvadba et al. 2008; Liu et al. 2013a, 2013b) quasars across low (e.g., Feruglio et al. 2010; Cicone et al. 2012; Feruglio et al. 2013; Rauch et al. 2013; Cicone et al. 2014) and high (e.g., Alexander et al. 2010; Nesvadba et al. 2011; Harrison et al. 2012, 2014; Carniani et al. 2015; Vayner et al. 2021b) redshift. These energetic outflows and jets emanating from the AGN may inflate galactic-scale bubble-like structure along the minor axis (largely perpendicular to the main plane of the galaxy) extending beyond tens of kiloparsecs (e.g., Leung et al. 2021), eventually expanding into the intergalactic medium. This is also referred to as a superbubble. Originally, superbubbles are powered by the combined explosions of supernovae in a cluster of massive stars, with cavities of diameter greater than 100 pc and density lower than that of the surrounding interstellar medium (ISM; Tenorio-Tagle & Bodenheimer 1988; Rupke & Veilleux 2013; Zaninetti 2021). The kinetic energy of the optical line–emitting gas may reach several times 10^{55} erg (Cecil et al. 2002). In the recent literature, this definition extends to AGN-inflated bubbles. A well-known local example is the nuclear superbubble emerging from the edge-on galaxy NGC 3079, although the central starburst appears sufficient to power the outflow with a contribution from the AGN (Irwin & Seaquist 1988; Veilleux et al. 1994; Cecil et al. 2001). A spectacular 10 kpc bipolar superbubble dominated by AGN radiation is detected in the radio, optical, and X-ray bands in the "Teacup AGN" (SDSS J1430+1339) at redshift $z = 0.085$ (Lansbury et al. 2018). So far, 10 kpc scale optical superbubbles driven by AGN have been found around obscured quasars at low redshift (e.g., Greene et al. 2012). Such spatially resolved cases through ionized emission line gas are still scarce.

Roughly 20% of the quasars show blueshifted broad absorption lines (BALs), implying that radiatively driven high-velocity outflows are ubiquitous (Proga et al. 2000; Hewett & Foltz 2003). Previous work found that such massive, subrelativistic outflows can be very efficient feedback agents, based on ultraviolet (UV) BAL analyses (McCarthy et al. 2010; Faucher-Giguère et al. 2012; Choi et al. 2014; Miller et al. 2020; Byun et al. 2022). A recent study using the large sample of Sloan Digital Sky Survey (SDSS) quasars (Rankine et al. 2020) concludes that BALs and non-BALs represent different views of the same underlying quasar population, implying that the outflows in BAL and non-BAL quasars are similar. In this work, we present the Very Large Telescope (VLT)/MUSE discovery of the powerful ionized gas outflow detected in a non-BAL quasar at $z \sim 0.6$.

The typical non-BAL quasar HE 0238−1904 has a central black hole of $2.4 \times 10^{10}\ M_{\odot}$ (Onken et al. 2004). Previous UV spectroscopy reported the detection of highly ionized collimated outflow in this source (Muzahid et al. 2012). Detailed modeling indicates that the outflow has two ionization phases, where the high-ionization phase carries the bulk of the material (Arav et al. 2013). The absorbing gas is blueshifted from the quasar, and the electron density is $n_e = 1.2 \times 10^{3.79\pm0.17}$ cm^{-3} measured by the $N_{\rm ion}({\rm O\,IV}^{*})/N_{\rm ion}({\rm O\,IV})$ ratio in the absorption troughs. The corresponding mass flux and kinetic luminosity are 40 $M_{\odot}$ yr^{-1} and 10^{45} erg s^{-1}, respectively, where the latter is roughly equal to 1% of the bolometric luminosity (Arav et al. 2013). Hence, this outflow is capable of strong interaction with the host galaxy. Nevertheless, all of these UV absorption line analysis results depend on detailed photoionization modeling and would benefit from spatially resolved studies.

This paper is structured as follows. We first describe the observations and data reduction in Section 2. In Sections 3 and 4, we present the analysis of the spectral data and measurements of the gas kinematics. In Section 5, we discuss the gas kinematics measured by integral field spectroscopy (IFS) and BAL analyses. We summarize our findings in Section 6. Throughout this paper, we adopt a cosmology with $H_0 = 70$ km s^{-1} Mpc^{-1}, $\Omega_m = 0.3$, and $\Omega_{\Lambda} = 0.7$. The redshift of HE 0238−1904 is adopted as $z = 0.631 \pm 0.001$, measured using Mg II λ2798 (Wisotzki et al. 2000) and consistent with values in recent papers (e.g., $z = 0.631$, Flesch 2015; Neeleman et al. 2016; $z = 0.629 \pm 0.002$, Muzahid et al. 2012).

2. Observations and Data Reduction

Between 2016 November and 2017 February, HE 0238–1904 was observed by VLT/MUSE under European Southern Observatory (ESO) program ID 096.A-0222(A) (PI: Schaye). The spectra were taken in the optical band (wavelength coverage $\lambda \sim 4750$–9350 Å in the observer's frame), covering 2912–5978 Å in the rest frame for our target at $z \sim 0.6$. The total on-source integration time is over 8 hr. The field of view approximately covers $1' \times 1'$ with a spatial resolution of $0\farcs8 \times 0\farcs8$ and a medium spectral resolution of $R = 3500$. The typical seeing is $0\farcs7$–$1\farcs2$, and the airmass ranges between ∼1.0 and ∼1.4.

After removing cosmic rays from the raw data using the L.A. Cosmic procedure (van Dokkum 2001), we reduce the raw data using the ESO-MUSE pipeline. The final data cubes have a spatial scale of $0\farcs2 \times 0\farcs2$. The estimated angular resolution is $\sim 0\farcs8$ based on the FWHM of the point-spread function (PSF) map, which roughly corresponds to a physical scale of 5.5 kpc at a redshift of $z = 0.631$. We estimate the instrumental PSF using the surface brightness profiles of broad emission lines (BELs), i.e., using a 2D Gaussian to fit the BEL map.

3. IFS Data Analysis

3.1. Multicomponent Gaussian Fitting

In order to understand the dynamics and main properties of the ionized outflows, we perform a kinematical analysis of the forbidden lines. We remove the BEL from the quasar nucleus, which is represented by double Gaussians in the spatial regions where the narrow emission lines are negligible. With the quasar contribution removed, we scrutinize the spatially resolved emission lines following the method described in Zhao et al. (2021).

We perform a two-step spectral fit to delineate the gas kinematics. First, we extract the spectrum in each spaxel and subtract the continuum using the interpolation method from wavelength on two sides of the [O III] line, where the continuum is free of any line emission and artifacts. We use the Fe II template from Tsuzuki et al. (2006) to subtract the Fe II emission. Second, we assume that the [O III] doublet is originating from the same upper level, and the intensity ratio is $I(5007)/I(4959) \sim 3$. The lines are fitted with the same central velocity and velocity dispersion. The profile of the [O III] λ5007 Å emission line is generally complex, so the [O III] $\lambda\lambda$4959, 5007 doublet is fitted with a combination of multiple Gaussians by minimizing χ^2 using the Python package `MPFIT`. We fit the [O III] profiles to no more than three Gaussians, following Liu et al. (2014).

The [O III] nebula surrounding HE 0238−1904 is spatially resolved by our IFS observation. The [O III] map of HE 0238−1904 is shown in Figure 1(a), where the false color is used to represent the intensity on a logarithmic scale. The surface brightness sensitivity (rms noise) of our [O III] maps is approximately $\sigma \sim 3 \times 10^{-19}$ erg s^{-1} cm^{-2} arcsec^{-2}. We use a 1.5σ threshold to create this map.

3.2. Nonparametric Measurements

We obtain nonparametric measurements of the emission line profiles following the method described in Liu et al. (2013a). These include the following.

1. Zeroth-moment map: intensity map of the [O III] λ5007 line.
2. First-moment map: $v_{\rm med}$, median velocity map.
3. Second-moment map: line width map, W_{80}, the velocity width of the line that encloses 80% of the total flux. This is defined as the difference between the velocities at 10% and 90% of cumulative flux: $W_{80} = v_{90} - v_{10}$.
4. Asymmetry: $A = \frac{(v_{90} - v_{\rm med}) - (v_{\rm med} - v_{10})}{W_{80}}$. With our definition, a profile with a significantly blueshifted wing has a negative A value, while a symmetric profile has $A = 0$.

We perform these nonparametric measurements on the best-fitting profiles. Figure 1 shows these parameters of the ionized gas derived from the fit of the [O III] λ5007 line. The maps are obtained by selecting only pixels with a signal-to-noise ratio (S/N) $\geqslant 1.5$.

4. Properties of the Outflow

4.1. Gas Kinematics

The forbidden emission line [O III] $\lambda\lambda$5007, 4969 doublet is adopted as a tracer of ionized outflows on large scales. Figure 1 shows the [O III] intensity, velocity, velocity dispersion, and asymmetry maps. Our IFS data confirmed that the [O III] λ5007 line is spatially and kinematically resolved. In the following, we discuss the velocity, velocity dispersion, and asymmetry of the ionized gas and compare them with previous works (e.g., Arav et al. 2013; Liu et al. 2013a; Carniani et al. 2015).

The velocity field of the [O III] nebula is remarkably well organized (Figure 1(b)). Only the blue-side outflows are detected, whereas the red side is probably obscured by the host galaxy along the line of sight. For this reason, the [O III] line profile is asymmetric, with a prominent blueshifted wing (Figures 1(d) and 2).

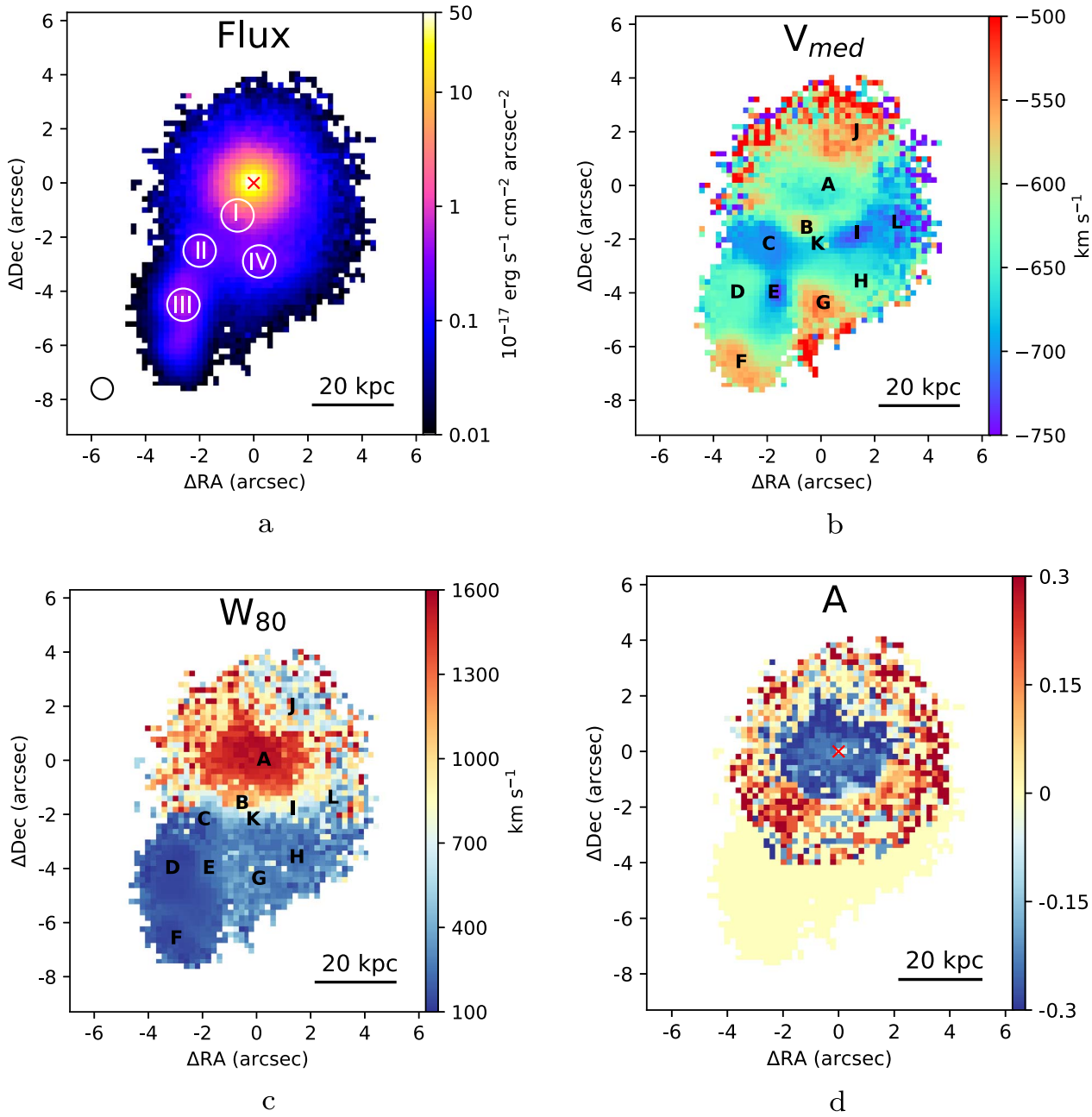

Figure 1. Nonparametric measurements of HE 0238−1904. The maps are (a) flux intensity of [O III] (erg s^{-1} cm^{-2} arcsec^{-2}), (b) median velocity (km s^{-1}), (c) line width (W_{80}; km s^{-1}), and (d) asymmetry (A). The maps were obtained by selecting only those spaxels with an S/N of the [O III] λ5007 line equal to or higher than 1.5. The red cross marks the position of the quasar. The PSF (0.″8) is depicted by the open circle in the lower left corner of panel (a).

We find the maximum W_{80} value of ∼1600 km s^{-1} in the center, which is comparable to that of known quasar outflows (e.g., Liu et al. 2013a; Carniani et al. 2015; Zakamska et al. 2016; Kubo et al. 2022) but considerably larger than the usual narrow lines in the quasar (Lonsdale et al. 1993). The W_{80} value drops to ∼200 km s^{-1} in the outer region. The asymmetry map shows regions with heavy blueshifted wings (<0) that are spatially associated with a high velocity dispersion (∼1600 km s^{-1}; see Figure 1(c)).

In Figure 1(d), we show the map of the asymmetry parameter A. The asymmetry parameter A is uniformly negative in the bright central part of HE 0238−1904, indicating heavily blueshifted wings in the line profiles. This is the telltale signature of an outflow that may be proceeding in a symmetric fashion but whose redshifted part is obscured by the material in the host galaxy or near the nucleus (Whittle 1985). In the fainter outer region where the peak S/N of even the brightest emission line [O III] is just a few, typically one Gaussian component is sufficient to fit the line profile. Therefore, the asymmetry parameter tends to be at zero values ($A = 0$).

Motivated by the different kinematic components apparent in the velocity map, we extract and fit the [O III] lines in 12 regions. Figures 1(b) and 2 show the position and spectra of these extraction regions, referred to as A–L. Regions A and B correspond to the position of the quasar itself and its immediate vicinity, while C–L correspond to the outer regions. The spectral fits reveal that the width of the line profile in the center is broader than that of the outer regions. The most significant

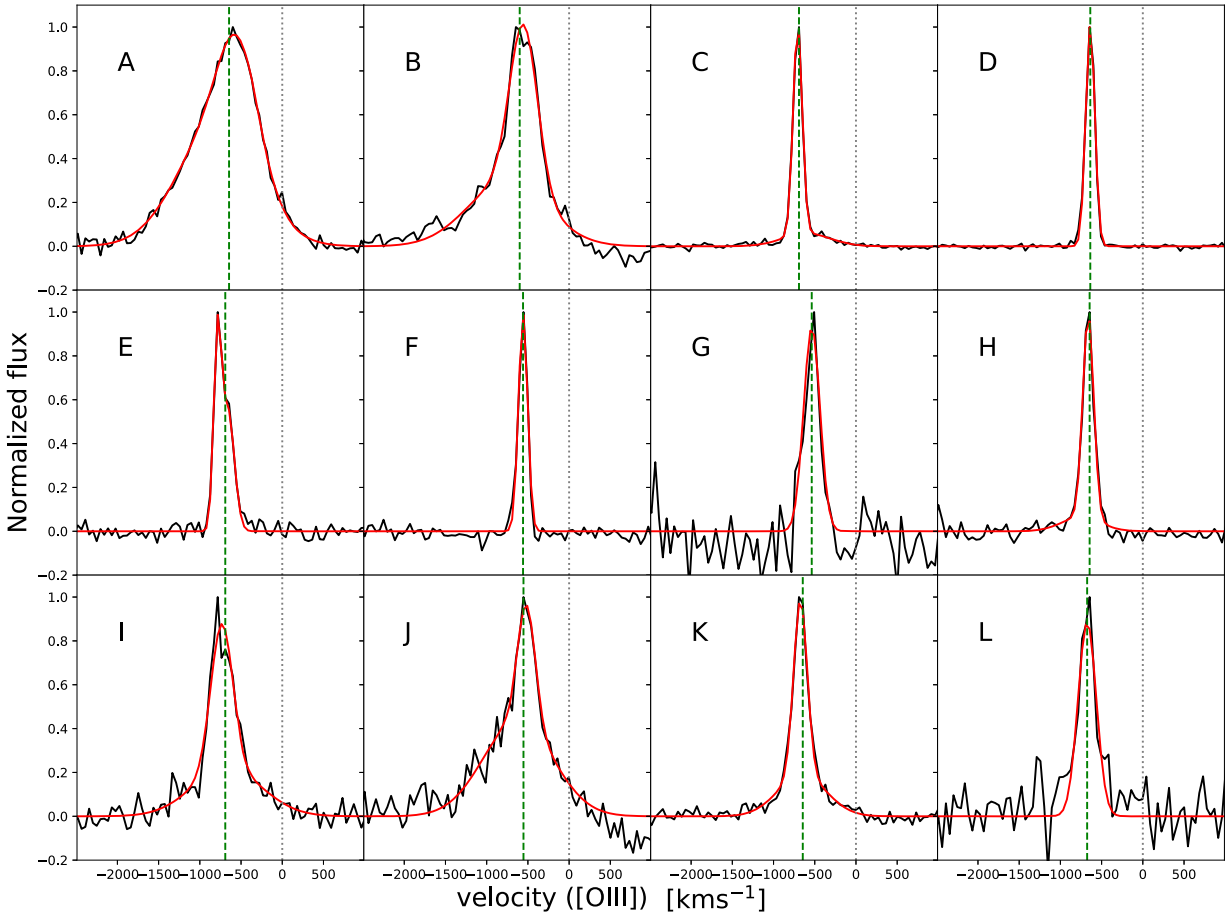

Figure 2. We select 12 spatial positions to illustrate the [O III] velocity profile therein, including central (A and B) and outer (C–L) regions as shown in Figure 1. The median and zero velocity are marked by green dotted and gray dashed lines, respectively.

asymmetry in the line profile is present in the center. Consequently, the smooth morphology of the [O III] nebula, the velocity, the high velocity dispersions of the gas, and the blueshifted asymmetry map all suggest that we have detected ionized outflowing gas in HE 0238−1904.

In Figure 3, we show values of W_{80} in all spaxels as a function of projected distance from the center. The radial profiles of W_{80} are almost flat at projected distances $R \lesssim 8$ kpc and appear to decrease at larger radii. This is different from previous results found in other quasars based on long-slit and IFS observations, which reported flat W_{80} profiles (Greene et al. 2011; Liu et al. 2013a). One of the concerns with the measured decline in W_{80} is that the broad component can no longer be identified in the outer parts, and the W_{80} measurement is due to the narrow component, hence the declining W_{80}. In this case, the W_{80} parameter would be almost constant across the nebulae in most cases, perhaps declining slightly toward the outer parts. This is not consistent with our W_{80} profile. The possible origin of the rapid decline in W_{80} is discussed in Section 5.1.

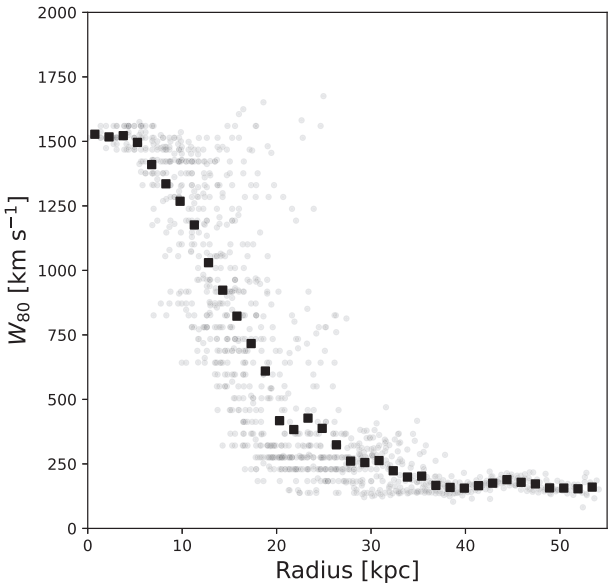

Figure 3. Radial dependence of W_{80}. Filled squares mark the mean of W_{80} in 1.5 kpc bins using the original data with an S/N of [O III] higher than 5. Gray points show the original data with an S/N of [O III] higher than 5.

4.2. The Spatially Resolved Blobs

The ionized gas extends to the southeast of the nucleus (see Figure 1), where three blobs (regions II–IV; Figure 1(a)) and a nuclear region (region I) are present. Both the velocity and the velocity dispersion of regions II–IV are similar ($v \sim 700$ km s^{-1}, $W_{80} \sim 400$ km s^{-1}).

The electron density can be derived from [O II] $I(3729)/I(3726)$ ratios. For this purpose, we stack the spectra taken from regions I–IV and fit the [O II] doublet emission lines by fixing the kinematics of the two lines (Figure 4). Assuming an

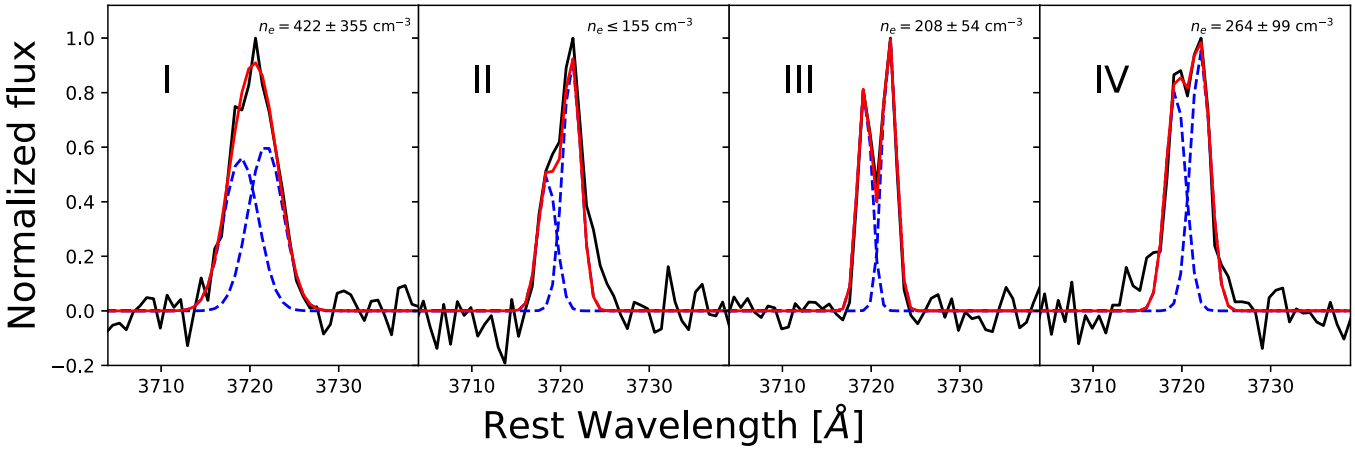

Figure 4. We select four spatial positions (Figure 1) to present the [O II] $\lambda\lambda$3737, 3729 doublet profiles. The observed spectra and fitted lines are in black and red, respectively, while the blue dotted lines are the Gaussian components. The electron density in region II is the upper limit in 3σ.

electron temperature of 10,000 K, we estimate the electron density to be $n_e = 422 \pm 355$, 208 ± 54, and 264 ± 99 cm^{-3} in regions I, III, and IV, respectively. The electron density in region II is $n_e \leqslant 155$ cm^{-3}, which is the upper limit at 3σ significance. This result is close to that of other quasar outflows (a few hundred per cubic centimeter; Nesvadba et al. 2006, 2008). Note that the [O II] doublet is blended together in the center and difficult to fit, so we stack and fit the spectra from the relatively outer region around the nucleus (region I). Hence, the actual electron density can be higher in the nuclear region.

5. Discussion

5.1. Origin of the Ionized Gas

There are two possibilities for the origin of the ionized gas. The gas can be either a nuclear outflow launched by AGN or a tidal tail due to galaxy interaction. First, the extended ionized gas is ubiquitous in quasars and generally driven by radiation pressure, so the ionized gas in HE 0238−1904 could well be the same. On the other hand, one could suspect that this spatially extended feature with a low velocity dispersion (regions II–IV) is in fact a tidal tail resulting from interaction with a lower-mass companion. We analyze all spectra of the companion galaxies around HE 0238−1904 in the field of view, and the difference between galaxy systemic velocity and this extended emission line gas velocity is found to be at least several hundred kilometers per second. This excludes the possibility of ionized gas being a tidal tail because the velocity difference between companion galaxies and tidal tails is generally $\lesssim$100 km s^{-1} (e.g., Fu et al. 2021).

In addition, the intensity ratios of the emission lines facilitate our analysis of the physical conditions of the ionized gas. Specifically, we use the [O III]/Hβ ratios to quantify the degree of ionization. To obtain higher S/Ns, we stack the spectra from regions II–IV shown in Figure 1(a). The Hβ and [O III] spectra and the [O III]/Hβ ratios in the extended regions (II–IV) are shown in Figure 5. In this object, Hβ almost follows the same spatial distribution as that of [O III] because [O III]/Hβ is almost a constant. The ratio reveals that [O III]/Hβ is close to 10 in these three regions, implying a high-ionization state in general. Based on the BPT diagram (Baldwin et al. 1981), [O III]/Hβ $>$ 10 implies AGN dominance. The [O III]/Hβ profile indicates that the AGN plays a dominant role in the ionization of the large-scale gas.

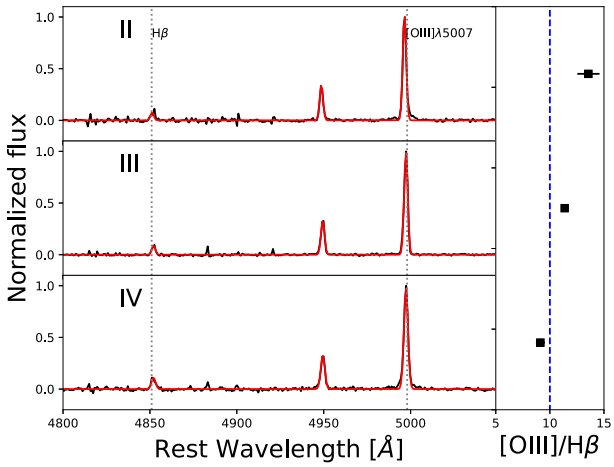

Figure 5. Left: spectra of the Hβ and [O III] doublet at three different regions (II–IV). The red line shows the best fit, and the black line shows the stacked spectra. Right: line ratio of [O III]/Hβ in three regions. The blue dashed line marks the typical [O III]/Hβ ratio. The ratio persists at a constant level ($\sim$10) in these three regions.

In Figure 3, we find that the W_{80} parameter is almost flat at projected distances $R \lesssim 8$ kpc and appears to decrease rapidly at larger radii. Here we discuss the possible origins of the rapid decline of W_{80} with increasing distance from the center. This decline of W_{80} implying an apparent narrowing of the line profile is likely due to the fact that the outflow becomes more directional or collimated within these structures. We thus confirm the previous results based on UV analyses that indicated collimated outflow (Muzahid et al. 2012).

There are various mechanisms capable of establishing an apparently declining W_{80} profile. First, in the central region, the wind expands in all directions from the quasar, whereas at larger distances, the opening angle of the outflow is decreased, perhaps because there are low-density regions along which the wind prefers to propagate. Also, the outflow in the central region may be experiencing large turbulent motions due to interaction with the ISM, but once they escape out of the inner galaxies, the flow becomes more organized and mostly radial. The episodic quasar outbursts may drive a shock wave through the ISM of the galaxy and clear out some of it (Novak et al.

2011). In any subsequent episodes, the wind suffers less resistance from the ISM and breaks out in these directions, producing the large-scale bubbles (Faucher-Giguère et al. 2012). Numerical simulations show that this phenomenon is expected for jet-driven winds (Sutherland & Bicknell 2007). We detected three spatially resolved blobs, which are likely part of the rim of the superbubble. In addition, the outflowing gas is launched and accelerated somewhere close to the quasar and proceeds ballistically. Thus, these outflowing gaseous blobs eventually slow down as they overcome the potential well of the host galaxy, producing a decline in W_{80}.

The ionized outflow traced by [O III] emission extends to 50 kpc and beyond, and W_{80} remains larger than 500 km s^{-1} up to 20 kpc (Figure 3). Combined with the large-scale morphology and the W_{80} profile, the extended gas we detected closely resembles a superbubble. Future high-quality soft X-ray observations are needed to fully investigate the origin of this ionized gas.

5.2. Energetics of the Outflow

We find that the ionized gas southwest of the nucleus extends to a projected distance reaching 55 kpc (Figure 1). Some characteristic parameters of the ionized gas are further estimated. We adopt a blueshifted velocity of $v_0 \sim 690$ km s^{-1} and a distance to the galaxy nucleus of $R_0 \sim 55$ kpc. We estimate a dynamical timescale to be $t \sim 7.8 \times 10^7$ yr, i.e., the time required for the gas from the nuclear region to reach such a distance with an average velocity of v_0. The mass of the gas can typically be estimated using Hβ luminosity $L_{\mathrm{H}\beta}$ and electron density n_e (e.g Liu et al. 2013a; Harrison et al. 2014). The total mass of this ionized extended gas can be derived as

$$\frac{M_{\mathrm{gas}}}{2.82 \times 10^9 M_\odot} = \left(\frac{L_{\mathrm{H}\beta}}{10^{43}\ \mathrm{erg\ s^{-1}}}\right)\left(\frac{n_e}{100\ \mathrm{cm^{-3}}}\right)^{-1}. \quad (1)$$

We take the electron density of $n_e \sim 400$ cm^{-3} in region I because the bulk of the ionized gas is concentrated in the central region. We find $L_{\mathrm{H}\beta} \sim 3.02 \times 10^{42}$ erg s^{-1} and $M_{\mathrm{gas}} \sim 2.1 \times 10^8\ M_\odot$. Combining with the average velocity of $v \sim 690$ km s^{-1}, the total kinetic energy of the gas can be estimated as

$$E_{\mathrm{kin}} = \frac{1}{2} M_{\mathrm{gas}} v_{\mathrm{gas}}^2 = 1.0 \times 10^{57}\ \mathrm{erg}. \quad (2)$$

We can also estimate that the mass outflow rate $\dot{M}$ is 2.7 $M_\odot$ yr^{-1}, and the kinetic energy rate is $\dot{E}_{\mathrm{kin}} \sim 4.1 \times 10^{41}$ erg s^{-1}. The momentum flux of the outflow ($\dot{P}_{\mathrm{outflow}} = \dot{M} \times v$) is 1.2×10^{34} dynes, or $\log(c\dot{P}_{\mathrm{outflow}}/L_\odot) = 10.9$. The ratio of the momentum flux of the outflow to the AGN radiation is only 0.002.

For effective feedback, theoretical modeling predicts that ~0.5%–5% of the AGN's bolometric luminosity is converted to the kinetic energy of the outflow (e.g., Hopkins & Elvis 2010). The kinetic luminosity of the outflow detected at 55 kpc is insignificant, only 0.0002% of its bolometric luminosity ($L_{\mathrm{bol}} = 10^{47.2}$ erg s^{-1}; Arav et al. 2013). This is much lower than the previously estimated $\dot{E}_{\mathrm{kin}}/L_{\mathrm{bol}} \sim 1\%$ from absorption on a 3 kpc scale (Arav et al. 2013) or the ~0.05%–0.1% estimated for a sample of $z \sim 2.4$ quasars (Carniani et al. 2015). Carniani et al. (2015) fit a log-linear relation between $\dot{M}$ and L_{bol} for the ionized outflows detected on kiloparsec scales in their quasar sample. Adopting their Equation (10), the expected $\dot{M} \sim 30 M_\odot$ yr^{-1} for HE 0238−1904 agrees fairly well with the derived $\dot{M} \sim 40 M_\odot$ yr^{-1} in Arav et al. (2013). In contrast, our estimated mass outflow rate at large scales (55 kpc) in HE 0238−1904 is an order of magnitude lower. The kinetic power of the outflow ($\ll 0.1\%$ L_{bol}) implies that it is no longer an important contributor to feedback at this scale.

5.3. Comparison with Previous UV Analysis

Using the HST/COS and FUSE UV spectra of HE 0238–1904, Muzahid et al. (2012) reported a detection of outflowing gas in multiple absorption lines: O VI, Ne VIII, and Mg X. They identified evidence for a similar covering factor in several absorption components that kinematically spread over ~1800 km s^{-1}, suggesting a collimated outflow. This is consistent with our expectation from the radial variation of W_{80}.

Determining the location of the absorption outflow is usually challenging. Nevertheless, assuming a spherical geometry, Muzahid et al. (2012) constrained the radial distance of the absorbing gas to be $R \sim 90$ pc based on the photoionization modeling result. The detailed UV absorption line analysis by Arav et al. (2013) was able to robustly derive a distance of $R \sim 3$ kpc from the outflow to the nucleus using absorption troughs of O IV and O IV*. As revealed by the MUSE data, the projected distance of the outflow from the AGN is $R \sim 55$ kpc for the blueshifted side. This is significantly further from the previous locations of the absorbing gas. In addition, both the electron density and the kinematics of these outflows determined from IFS of emission lines are different from those derived from previous UV absorption line analyses (e.g., Arav et al. 2013). The velocity of the absorption line (~5000 km s^{-1}) is much higher than the velocity of the emission line (~700 km s^{-1}). This strongly indicates that the outflows detected using the absorption and emission lines are clearly not the same component but likely stratified components of different spatial scale and velocity in the ionized phase outflow.

6. Summary

In this paper, we present VLT/MUSE IFS observations of the non-BAL quasar HE 0238–1904 at redshift $z = 0.631$. The [O III] emission lines are characterized by large line widths and prominent blue wings in the center, indicative of fast outflows accelerated by the powerful AGN. We summarize our results as follows.

1. For the first time, we identify a spatially and kinematically resolved superbubble driven by AGN at intermediate redshift. From the emission line map, ionizing structure, and kinematics, we identify a spatially resolved superbubble surrounding HE 0238−1904, showing a one-sided structure reaching a projected distance of $R \sim 55$ kpc from the nucleus. We calculate an electron density n_e of a few hundred per cubic centimeter for three blobs and the central region. The electron density in the center is higher than that in the outer regions. The velocity of the ionized gas is blueshifted ~700 km s^{-1}, with a rapid decline in the radial profile of W_{80}.
2. We estimate $M_{\mathrm{gas}} \sim 2.1 \times 10^8\ M_\odot$ for the ionized gas mass. The dynamical timescale of the blobs is estimated to be ~78 Myr, the travel time of the clouds from the

center to reach the observed distance. The resulting mass outflow rate is 2.7 $M_{\odot}$ yr^{-1}. The kinetic energy carried by the ionized gas is 1.0×10^{57} erg, with an estimated kinetic energy rate $\dot{E}_{\rm kin} \sim 4.1 \times 10^{41}$ erg s^{-1}. Feedback in HE 0238–1904 is taking place on kiloparsec scales as previously reported, but the outflow on the 55 kpc scale is inadequate to effectively regulate the evolution of its host galaxy (the kinetic luminosity is only 0.0002% of the bolometric luminosity).

3. The inferred mass flow rate and kinetic luminosity of the outflow are different from that of a previously identified absorption system. The outflows detected in absorption and emission lines are most likely stratified components at different spatial scales and velocities.

We thank the anonymous referee for helpful suggestions that significantly improved our work. We thank the Guilin Liu, Zesen Lin, and Luming Sun for helpful discussion. We acknowledge support by NSFC grants U1831205, 12033004, and 12221003 and the science research grants from the China Manned Space Project, CMS-CSST-2021-A06 and CMS-CSST-2021-B02. This research has made use of the services of the ESO Science Archive Facility. Based on observations collected at the ESO under program 096.A-0222(A).

ORCID iDs

Junfeng Wang https://orcid.org/0000-0003-4874-0369

References

Alexander, D. M., Swinbank, A. M., Smail, I., McDermid, R., & Nesvadba, N. P. H. 2010, MNRAS, 402, 2211
Arav, N., Borguet, B., Chamberlain, C., Edmonds, D., & Danforth, C. 2013, MNRAS, 436, 3286
Baldwin, J. A., Phillips, M. M., & Terlevich, R. 1981, PASP, 93, 5
Byun, D., Arav, N., & Hall, P. B. 2022, MNRAS, 517, 1048
Carniani, S., Marconi, A., Maiolino, R., et al. 2015, A&A, 580, A102
Cecil, G., Bland-Hawthorn, J., & Veilleux, S. 2002, ApJ, 576, 745
Cecil, G., Bland-Hawthorn, J., Veilleux, S., & Filippenko, A. V. 2001, ApJ, 555, 338
Choi, E., Naab, T., Ostriker, J. P., Johansson, P. H., & Moster, B. P. 2014, MNRAS, 442, 440
Choi, E., Ostriker, J. P., Naab, T., & Johansson, P. H. 2012, ApJ, 754, 125
Cicone, C., Feruglio, C., Maiolino, R., et al. 2012, A&A, 543, A99
Cicone, C., Maiolino, R., Sturm, E., et al. 2014, A&A, 562, A21
Croton, D. J., Springel, V., White, S. D. M., et al. 2006, MNRAS, 365, 11
Di Matteo, T., Springel, V., & Hernquist, L. 2005, Natur, 433, 604
Faucher-Giguère, C.-A., Quataert, E., & Murray, N. 2012, MNRAS, 420, 1347
Ferrarese, L., & Merritt, D. 2000, ApJL, 539, L9
Feruglio, C., Fiore, F., Maiolino, R., et al. 2013, A&A, 549, A51
Feruglio, C., Maiolino, R., Piconcelli, E., et al. 2010, A&A, 518, L155
Flesch, E. W. 2015, PASA, 32, e010
Fu, Z. X., Sengupta, C., Sethuram, R., et al. 2021, RAA, 21, 043
Gebhardt, K., Bender, R., Bower, G., et al. 2000, ApJL, 539, L13
Greene, J. E., Zakamska, N. L., Ho, L. C., & Barth, A. J. 2011, ApJ, 732, 9
Greene, J. E., Zakamska, N. L., & Smith, P. S. 2012, ApJ, 746, 86
Harrison, C. M., Alexander, D. M., Mullaney, J. R., & Swinbank, A. M. 2014, MNRAS, 441, 3306
Harrison, C. M., Alexander, D. M., Swinbank, A. M., et al. 2012, MNRAS, 426, 1073
Hewett, P. C., & Foltz, C. B. 2003, AJ, 125, 1784
Hopkins, P. F., & Elvis, M. 2010, MNRAS, 401, 7
Hopkins, P. F., Hernquist, L., Cox, T. J., et al. 2006, ApJS, 163, 1
Irwin, J. A., & Seaquist, E. R. 1988, ApJ, 335, 658
Kormendy, J., & Ho, L. C. 2013, ARA&A, 51, 511
Kubo, M., Umehata, H., Matsuda, Y., et al. 2022, ApJ, 935, 89
Lansbury, G. B., Jarvis, M. E., Harrison, C. M., et al. 2018, ApJL, 856, L1
Leung, G. C. K., Coil, A. L., Rupke, D. S. N., & Perrotta, S. 2021, ApJ, 914, 17
Liu, G., Zakamska, N. L., & Greene, J. E. 2014, MNRAS, 442, 1303
Liu, G., Zakamska, N. L., Greene, J. E., Nesvadba, N. P. H., & Liu, X. 2013a, MNRAS, 436, 2576
Liu, G., Zakamska, N. L., Greene, J. E., Nesvadba, N. P. H., & Liu, X. 2013b, MNRAS, 430, 2327
Lonsdale, C. J., Barthel, P. D., & Miley, G. K. 1993, ApJS, 87, 63
McCarthy, I. G., Schaye, J., Ponman, T. J., et al. 2010, MNRAS, 406, 822
Miller, T. R., Arav, N., Xu, X., & Kriss, G. A. 2020, MNRAS, 499, 1522
Muzahid, S., Srianand, R., Savage, B. D., et al. 2012, MNRAS, 424, L59
Neeleman, M., Prochaska, J. X., Ribaudo, J., et al. 2016, ApJ, 818, 113
Nesvadba, N. P. H., Lehnert, M. D., De Breuck, C., Gilbert, A. M., & van Breugel, W. 2008, A&A, 491, 407
Nesvadba, N. P. H., Lehnert, M. D., Eisenhauer, F., et al. 2006, ApJ, 650, 693
Nesvadba, N. P. H., Polletta, M., Lehnert, M. D., et al. 2011, MNRAS, 415, 2359
Novak, G. S., Ostriker, J. P., & Ciotti, L. 2011, ApJ, 737, 26
Onken, C. A., Ferrarese, L., Merritt, D., et al. 2004, ApJ, 615, 645
Proga, D., Stone, J. M., & Kallman, T. R. 2000, ApJ, 543, 686
Rankine, A. L., Hewett, P. C., Banerji, M., & Richards, G. T. 2020, MNRAS, 492, 4553
Rauch, M., Becker, G. D., Haehnelt, M. G., Carswell, R. F., & Gauthier, J.-R. 2013, MNRAS, 431, L68
Rupke, D. S. N., & Veilleux, S. 2013, ApJ, 768, 75
Silk, J., & Rees, M. J. 1998, A&A, 331, L1
Springel, V., Di Matteo, T., & Hernquist, L. 2005, MNRAS, 361, 776
Sutherland, R. S., & Bicknell, G. V. 2007, ApJS, 173, 37
Tabor, G., & Binney, J. 1993, MNRAS, 263, 323
Tenorio-Tagle, G., & Bodenheimer, P. 1988, ARA&A, 26, 145
Tremaine, S., Gebhardt, K., Bender, R., et al. 2002, ApJ, 574, 740
Tsuzuki, Y., Kawara, K., Yoshii, Y., et al. 2006, ApJ, 650, 57
van Dokkum, P. G. 2001, PASP, 113, 1420
Vayner, A., Wright, S. A., Murray, N., et al. 2021a, ApJ, 919, 122
Vayner, A., Zakamska, N. L., Riffel, R. A., et al. 2021b, MNRAS, 504, 4445
Veilleux, S., Cecil, G., Bland-Hawthorn, J., et al. 1994, ApJ, 433, 48
Veilleux, S., Cecil, G., & Bland-Hawthorn, J. 2005, ARA&A, 43, 769
Veilleux, S., Maiolino, R., Bolatto, A. D., & Aalto, S. 2020, A&ARv, 28, 2
Whittle, M. 1985, MNRAS, 216, 817
Wisotzki, L., Christlieb, N., Bade, N., et al. 2000, A&A, 358, 77
Zakamska, N. L., Hamann, F., Pâris, I., et al. 2016, MNRAS, 459, 3144
Zaninetti, L. 2021, IJAA, 11, 370
Zhao, Q., Sun, L., Shen, L., et al. 2021, ApJ, 913, 111